ACS Energy LETTERS

http://pubs.acs.org/journal/aelccp

LETTER

Two-Dimensional Material Interface Engineering for Efficient Perovskite Large-Area Modules

Antonio Agresti,[†,‡,¶] Sara Pescetelli,[†,¶] Alessandro Lorenzo Palma,[†] Beatriz Martín-García,[§,∥] Leyla Najafi,[§] Sebastiano Bellani,[§] Iwan Moreels,[∥] Mirko Prato,[⊥] Francesco Bonaccorso,*[,§,#] and Aldo Di Carlo*[,†,‡]

[†]CHOSE - Centre for Hybrid and Organic Solar Energy, Department of Electronic Engineering, University of Rome Tor Vergata, via del Politecnico 1, 00133 Rome, Italy

[‡]LASE – Laboratory of Advanced Solar Energy, National University of Science and Technology "MISiS", Moscow 119049, Russia

[§]Graphene Laboratories, Istituto Italiano di Tecnologia, via Morego 30, 16163 Genova, Italy

[∥]Nanochemistry Department, Istituto Italiano di Tecnologia, via Morego 30, 16163 Genova, Italy

[⊥]Materials Characterization Facility, Istituto Italiano di Tecnologia, via Morego 30, 16163 Genova, Italy

[#]BeDimensional S.p.A., Via Albisola 121, 16163 Genova, Italy

S *Supporting Information*

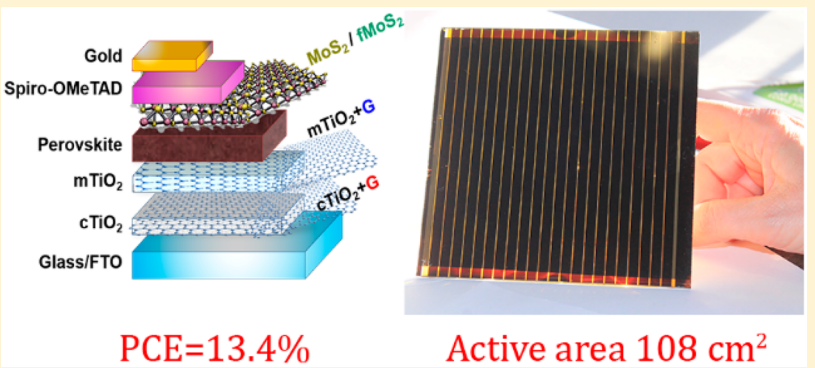

ABSTRACT: **In this work, we demonstrate the successful application of two-dimensional (2D) materials, i.e., graphene and functionalized MoS_2, in perovskite solar cells (PSCs) by interface engineering the standard mesoscopic n−i−p structure. The use of 2D materials has the dual role to improve both the stability and the overall power conversion efficiency (PCE) of the PSCs compared to standard devices. The application of 2D materials is successfully extended to large-area perovskite solar modules (PSMs), achieving PCEs of 13.4% and 15.3% on active areas of 108 cm^2 and 82 cm^2, respectively. This performance results in record-high active area-indexed aperture PCE (AIAPCE) of 1266.5% cm^2. In addition, the 2D materials-based PSMs show a stability under a prolonged (>1000 h) thermal stress test at 65 °C (ISOS-D2), representing a crucial advancement in the exploitation of perovskite photovoltaic technology.**

In recent years, lead-halide perovskite solar cells (PSCs) have catalyzed the attention of the scientific community, with power conversion efficiency (PCE) exceeding 20%, by using cost-effective and potentially scalable solution processing approaches.[1,2] In particular, the global research effort boosted the PCE of PSCs up to 24.2% for single-junction[3] and 27.3% for tandem perovskite/silicon[4] solar cells. Despite these important achievements, long-term stability[5] and scalability[6] are still the major constraints for the market entry of the perovskite photovoltaic technology.[7,8] In fact, the photoactive lead-halide perovskites typically lack stability due to their hygroscopicity and propensity to back-convert into their precursors during exposure to moisture,[9] oxygen,[10,11] and light illumination.[10,12] Moreover, they experience a tetragonal-to-cubic phase transition at the temperature reached during typical solar cell operation (>80 °C),[13] resulting in making them unfit for standard solar module certifications.[14,15] In addition, the deposition of both pin-hole-free homogeneous

Received: May 27, 2019
Accepted: June 27, 2019
Published: June 27, 2019

DOI: 10.1021/acsenergylett.9b01151
ACS Energy Lett. XXXX, XXX, XXX−XXX

high-crystallinity perovskite films and effective charge transport layers (CTLs) by industrial approaches is still a tough obstacle toward the development of large-area PSCs with PCE comparable to those achieved by lab-scale (less than few cm^2) cells.[16−18] In particular, the nucleation and crystal growth kinetics for high-quality perovskite film are attained by optimizing the choice of the solvent[19,20] and the solvent drying rate[21] and possibly using antisolvent crystallization.[22,23] However, this optimization pathway could not straightforwardly meet the requirements of large-area linear and/or roll-to-roll (R2R) coatings[24] (e.g., doctor blading[25] and gravure printing,[26] as well as slot-die and spray coating[27−29]). Beyond the issues relating to the perovskite layer, the choice of the architecture and the interface engineering of the PSCs also play a crucial role in achieving valuable upscaling criteria, since pinhole-free, homogeneous, and, eventually, compact CTLs are mandatory to reduce PCE losses,[30−34] i.e., to improve the extraction of the photogenerated charge carriers (i.e., the short circuit current density, J_{sc}, and the open-circuit voltage, V_{OC}).[35] Thereby, both n−i−p planar[7,36] and mesoscopic architectures[37,38] have been investigated for the realization of large-area PSCs and perovskite solar modules (PSMs),[16] as also reported by several PV companies (e.g., Microquanta Semiconductor, Solliance, Saule Technologies, and Greatcell Solar, just to cite a few). In favor of the planar structures, these can be produced through low-temperature material deposition processes (<180 °C), which make feasible the realization of flexible devices produced by using high-throughput R2R techniques.[39] So far, the largest solution-processed and efficient PSMs (e.g., aperture area = 16.07 cm^2 and PCE = 14.9%)[40] are based on planar n−i−p architecture, as obtained by depositing a tin oxide (SnO_2)-based electron transport layer (ETL) via spin[41]/slot-die coating,[40] and 2,2′,7,7′-tetrakis(*N*,*N*-di-4-methoxyphenylamino)-9,9′-spirobifluorene (spiro-OMeTAD)-based hole transport layer (HTL) via doctor blading[41]/spin coating.[40] Moreover, a planar architecture based on a SnO_2 ETL and carbazole derivative HTL, demonstrating remarkable stability under 70 mW/cm^2 in the case of small area devices,[42] achieved a PCE of 14.9% stable over 100 h in a 7.25 cm^2 active area mini-module.[43] By replacing SnO_2 with a compact TiO_2 ($cTiO_2$) ETL, as realized by means of high temperature (450 °C) spray pyrolysis deposition[44] or e-beam evaporation,[45] PCE losses have been further reduced to reach a remarkable PCE > 17% on 10.36 cm^2 active area[44] and a PCE > 10% on an active area of ∼170 cm^2.[45] Recently, PSMs based on inverted planar p−i−n architectures have also been produced via electrochemically assembling metal-filamentary nanoelectrodes.[46] Although these innovative PSMs exhibited a PCE exceeding 14% and a remarkable stability (PCE loss of ∼20% after >180 h at 85 °C and 85% humidity rate, HR), their active area was limited to 9.06 cm^2,[40,41,44,45] indicating the need to confirm their prompt and facile upscaling. Overall, the aforementioned examples have demonstrated that the planar architectures still face several issues that need to be overcome to design and realize large-area solution processed PSMs with high PCEs. Therefore, it is not by chance that the best performing (both in terms of PCE and stability) large area PSMs (size > 40 cm^2) have been demonstrated by using mesoporous architectures.[17,47] In particular, carbon-based PSMs[48,49] promise low-cost and superior stability in air compared to their counterparts based on metal contacts.[48,49] For example, carbon-based PSMs, produced by infiltrating perovskite over $cTiO_2$/mesoporous TiO_2 ($mTiO_2$)/zirconium oxide (ZrO_2)/carbon paste stacks, having an active area of 47.6 cm^2, have exhibited a stable PCE of 10.1% over more than 10 000 h under 1 sun illumination.[33] However, when the carbon structure was further scaled up to a record-high active area of 198 cm^2, the PCE dropped significantly (i.e., 6.6%)[50] due to the irregular infiltration process of the perovskite film. Meanwhile, traditional mesoscopic architectures with metal contacts have been reported for PSMs with record-high PCEs,[17] achieved by engineering the interfaces between the different composing layers. In particular, the interface engineering based on two-dimensional (2D) materials has recently been proposed as an effective way to improve the PCE and the stability of solution-processed PSCs.[51,52] For example, we have recently proposed graphene interface engineering (GIE) as a strategy to demonstrate PSMs with a PCE of 12.6% on an active area of 50 cm^2.[53] Here, GIE consists of using graphene and graphene-related materials (GRM) in the form of interlayers (also named active buffer layers, ABLs) at perovskite/CTL interfaces and/or as dopant for standard CTLs.[30,54−58] Previous investigations on mesoscopic n−i−p architectures (glass/fluorine tin oxide (FTO)/$cTiO_2$/graphene-doped $mTiO_2$ ($mTiO_2$+G)/perovskite/spiro-OMeTAD/gold (Au)) have demonstrated that graphene flakes incorporated into the $mTiO_2$ have a bifunctional role. On the one hand, they improve the perovskite morphology by reducing the density of the trap states located at the $mTiO_2$/perovskite interface,[54,55] thus limiting the irreversible dissociation of perovskite materials.[59] On the other hand, they promote the electron extraction from the perovskite to the ETL, as well as the electron transport within the ETLs toward the current collector (i.e., the FTO).[55] Despite the use of graphene being able to retard the degradation of the perovskite/ETL interface, the instability of the methylammonium lead iodide perovskite ($MAPbI_3$) still represented a limit to pass the standard stress test condition defined by the C450 testing protocol for photovoltaic modules.[60,61] In fact, $MAPbI_3$ undergoes a fast degradation upon exposure to moisture, due to its low formation energy, which causes its decomposition to solid PbI_2 and gaseous methylamine and hydrogen halide under moderate temperature (60 °C) stresses.[62] Furthermore, perovskite heating under operating conditions has been reported, causing degradation pathways attributed to atom migration from the Au electrode toward $MAPbI_3$.[22,27] In fact, Au, as well as other electrode metals, can react with $MAPbI_3$, creating nonradiative recombination centers, i.e., PCE losses.[63] Finally, voltage bias and/or thermal drift also cause the movements of ions composing $MAPbI_3$, inducing defects (e.g., iodine vacancies)[64,65] that degrade the interface of the device until its failure.[59]

With the aim to thermally stabilize the most efficient PSCs (as well as the corresponding PSMs), several perovskite absorber optimizations and new device architecture engineering strategies have been proposed.[66] First, thermally stable mixed-cation hybrid lead halide perovskites using methylammonium (MA), formamidinium (FA), and cesium (Cs) cations have been successfully designed by tuning the Goldschmidt tolerance factor.[67] Second, novel hole transport materials have been screened for stabilizing perovskite/HTL interfaces.[61,68] In fact, the well-known weak adhesion of the most established mild organic hole transport materials (e.g., spiro-OMeTAD or poly(triarylamine), PTAA) to the perovskite surface[69,70] can trigger PCE losses.[71] In addition, the poor hole mobility of the spiro-OMeTAD (in the order of 10^{-4} cm^2

DOI: 10.1021/acsenergylett.9b01151
ACS Energy Lett. XXXX, XXX, XXX−XXX

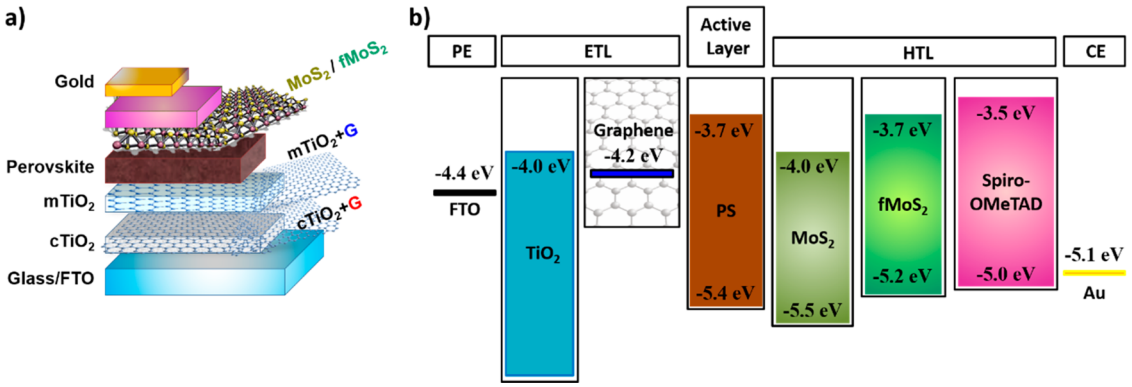

Figure 1. (a) 2D material-engineered PSC architecture and (b) its energy band diagram. The work function values for FTO, TiO_2, and graphene have been taken from refs 77−79. The highest occupied molecular orbital (HOMO) and lowest unoccupied molecular orbital (LUMO) levels for perovskite and spiro-OMeTAD have been taken from refs 80−82, respectively. The energy band edge positions for MoS_2 and $fMoS_2$ have been experimentally determined by optical absorption spectroscopy and ultraviolet photoelectron spectroscopy measurements, as detailed in the Supporting Information.

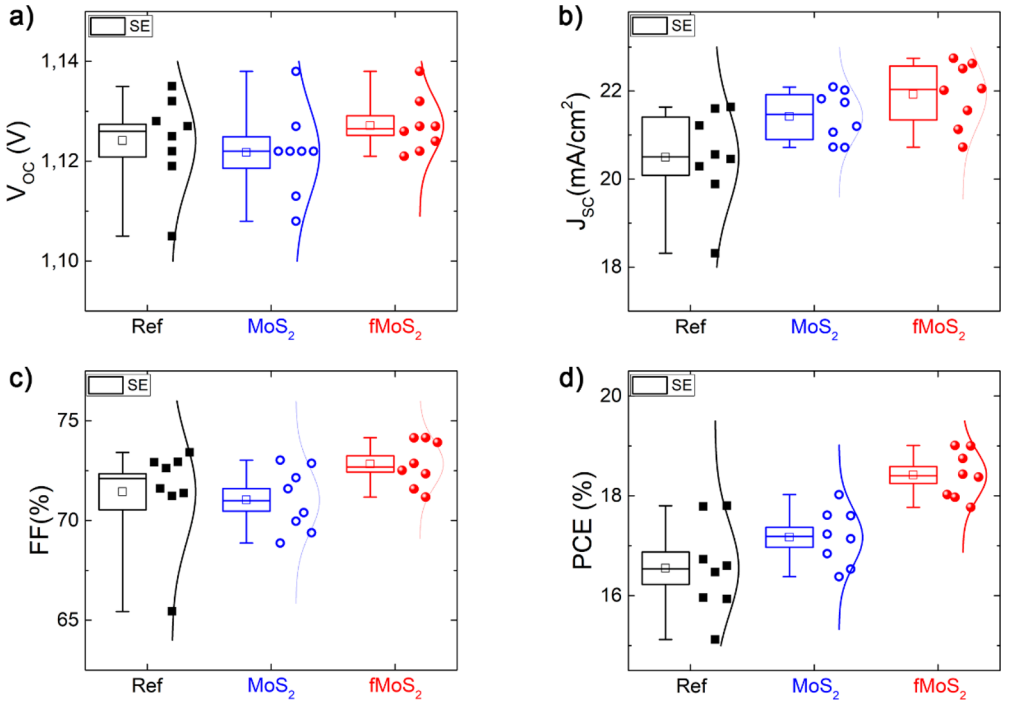

Figure 2. Photovoltaic parameter statistics for the investigated PSCs extracted by the *I*−*V* characteristics under 1 sun illumination: (a) V_{OC}, (b) J_{SC}, (c) FF, and (d) PCE. The statistics were measured on 8 PSCs for each architecture.

V^{-1} s^{-1})[72,73] requires the use of redox active p-type dopants, such as Li-bis(trifluoromethanesulfonyl)imide (Li-TFSI),[73] which intensify the device degradation because of their propensity to absorb moisture from the air and become dissolved in the moisture itself.[74] The photo-oxidation[75] and the crystallization at temperature > 80 °C[76] of spiro-OMeTAD can further damage its properties. To eliminate such issues, inorganic hole transport materials, such as copper thiocyanate (CuSCN),[61,68] have shown improved thermal[68] and light soaking stability relative to those of organic materials.[61] However, the hazardous solvents (e.g., diethyl sulfide) usually used to disperse CuSCN[61] require a well-controlled environment for the subsequent material deposition, increasing the associated costs in large-scale production chains.

In this work, we report the combination of thermally stable mixed-cation perovskite with 2D material-engineered mesoscopic n−i−p architecture as an effective method to design and realize PSMs. In particular, graphene-based ETLs are exploited to accelerate the electron extraction/collection, as well as to control the perovskite morphology over the mesoscopic scaffold. Furthermore, chemically functionalized molybdenum disulfide ($fMoS_2$) is used as an efficient ABL at the perovskite/HTL interface for improving the hole injection/collection at the counter-electrode (CE). A thermal-assisted spray coating technique is exploited to deposit $fMoS_2$ ABL without damaging the underlying perovskite film. Our 2D material-engineered PSMs have shown a PCE of 13.4% and 15.3% on active areas of 108 cm^2 and 82 cm^2, respectively. Moreover, the use of 2D materials allows the PSMs to achieve a satisfactory lifetime, displaying a PCE retention of 75%, under prolonged thermal stress at 65 °C (ISOS-D2) over the first 1000 h,

DOI: 10.1021/acsenergylett.9b01151
ACS Energy Lett. XXXX, XXX, XXX−XXX

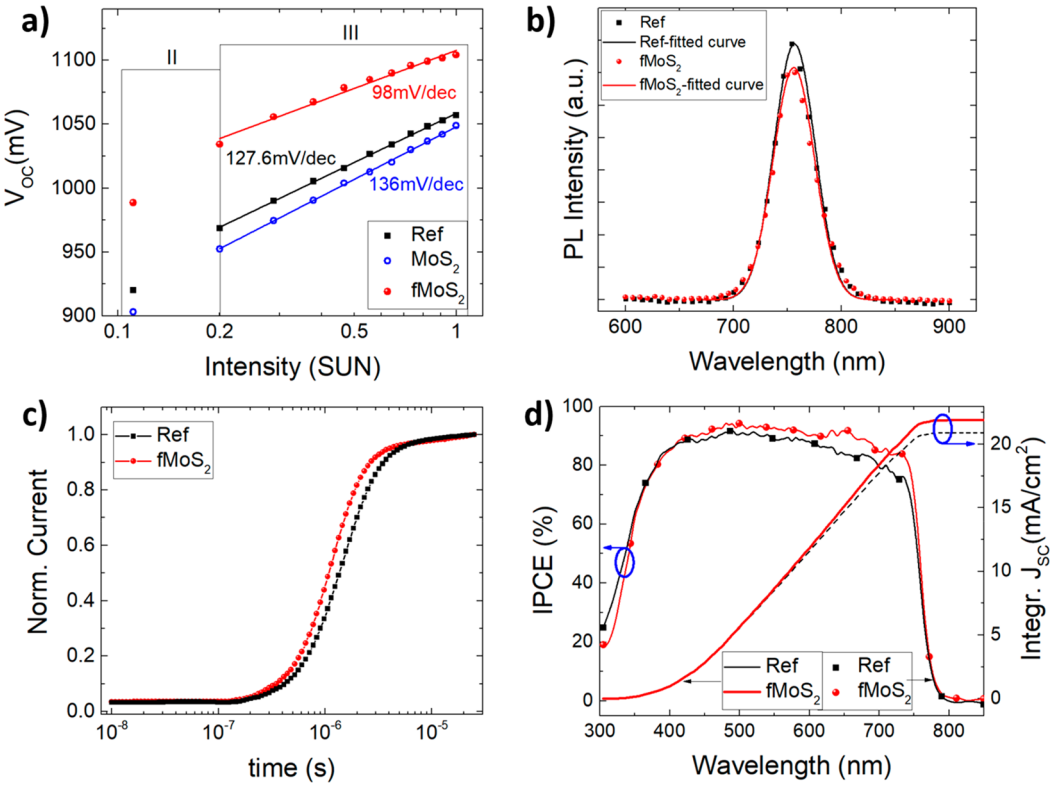

Figure 3. Transient and electro-optical analysis on as-produced PSCs. (a) V_{OC} vs log(P_{inc}) plot for the different devices with and without ABLs. (b) Photoluminescence (PL) emission from the devices without Au CE. (c) Transient photocurrent profile acquired by switching on the LED light for $fMoS_2$-based and reference devices. (d) Incident-photon-to-current conversion efficiency (IPCE) spectra and the corresponding integrated J_{SC} for $fMoS_2$-based and reference devices. All the measurements in (c) and (d) are acquired on complete devices.

confirming the crucial role of 2D material-based layers in preventing perovskite/CTL interface degradation.

Small-Area Devices. The proposed 2D material-engineered PSC architecture is depicted in Figure 1a, the following are the details: glass/FTO/$cTiO_2$+G)/$mTiO_2$+G/perovskite/spiro-OMeTAD/MoS_2 or $fMoS_2$/Au. The graphene-doped $cTiO_2$ ($cTiO_2$+G) layer was deposited by the same spray pyrolysis protocol from the $cTiO_2$ dispersion doped with graphene ink (1 vol %) dispersed in a mix of ethanol and water (80:20, v/v), while $fMoS_2$ (dispersed in 2-propanol) ABL was uniformly sprayed on large-area substrates by a thermal-assisted spray coating technique. More in detail, during the spray deposition, the module substrates were kept at 80 °C to speed up the evaporation of the $fMoS_2$ ink solvent and to prevent the perovskite degradation, in agreement with protocols previously reported.[30] The experimental details regarding the device manufacturing and the characterization tools used for device analysis are reported in the Supporting Information.

In particular, the prototypical ETL ($cTiO_2$/$mTiO_2$) was modified by the addition of graphene flakes into both the $cTiO_2$ ($cTiO_2$+G) and the $mTiO_2$ ($mTiO_2$+G). As reported in our previous works,[83] the insertion of graphene flakes into the $cTiO_2$ decreases the series resistance of the cell, which consequently exhibits high fill factor, FF (typically >75%), compared to the reference without graphene flakes.[84] Actually, the graphene flakes provide effective electrically conductive pathways to transport the electron toward the FTO electrode. Alongside, the addition of the graphene flakes into the $mTiO_2$ improves the device PCE by increasing both the FF and short circuit current (I_{SC}).[53] In agreement with steady-state photoluminescence (PL) and time-resolved photoluminescence (TRPL) spectroscopy measurements, the perovskite optimally crystallizes when it is wrapped into the $mTiO_2$+G, enhancing the electron injection efficiency at the $mTiO_2$+G/perovskite interface.[55] Theoretical simulations have also evidenced a ferroelectric distortion of the perovskite in contact with graphene, which drives electron extraction from the perovskite and hinders electron−hole recombination.[85] Meanwhile, the presence of graphene in the bare $mTiO_2$ layer improves the overall electron transport toward the $cTiO_2$, decreasing the series resistance and, thus, the FF of the device.[55] As a further step for the realization of efficient PSCs, an appropriate energy level tailoring at the perovskite/HTL interface is pivotal to improve the hole extraction for the perovskite to the HTL, eventually impeding the interface degradation induced by charge trapping phenomena.[59] In this context, several 2D material-based films, mainly transition metal dichalcogenides (TMDs), have been proposed as effective ABLs at the perovskite/HTL interface.[59,86−88] Among them, we exploited MoS_2 flakes, as obtained by liquid phase exfoliation (LPE) of bulk crystals in 2-propanol (see Supporting Information, Figure S1). The as-produced dispersion can be deposited over perovskite as an ABL by thermal-assisted spray coating (resulted by heating the substrate at 80 °C).[84,89] However, the MoS_2 valence band edge does not perfectly match with the perovskite highest occupied molecular orbital (HOMO) level and possibly forms an energy barrier for the hole extraction process. To avoid this drawback, we have also produced chemically functionalized MoS_2 flakes ($fMoS_2$), by linking thiol of 3-mercaptopropionic acid (MPA) moieties to the MoS_2 surface via S−S van der Waals physisorption[90] and/or S-vacancy passivation.[91,92]

DOI: 10.1021/acsenergylett.9b01151
ACS Energy Lett. XXXX, XXX, XXX−XXX

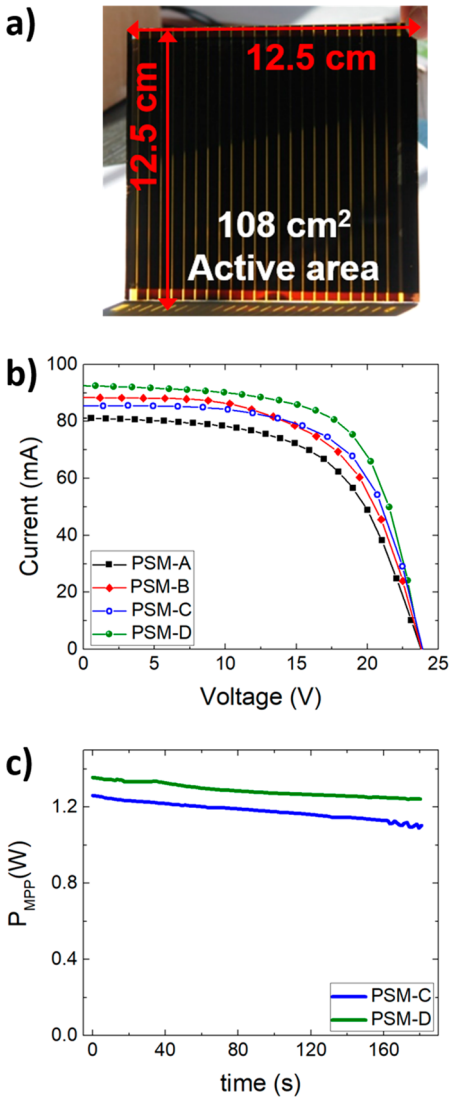

Figure 4. (a) Photograph of a representative large-area PSM (108 cm^2 active area, 156.25 cm^2 substrate area). (b) $I-V$ characteristics of tested PSMs. (c) Stabilized power at maximum power point (P_{MPP}) under 1 sun illumination for PSM-C and PSM-D.

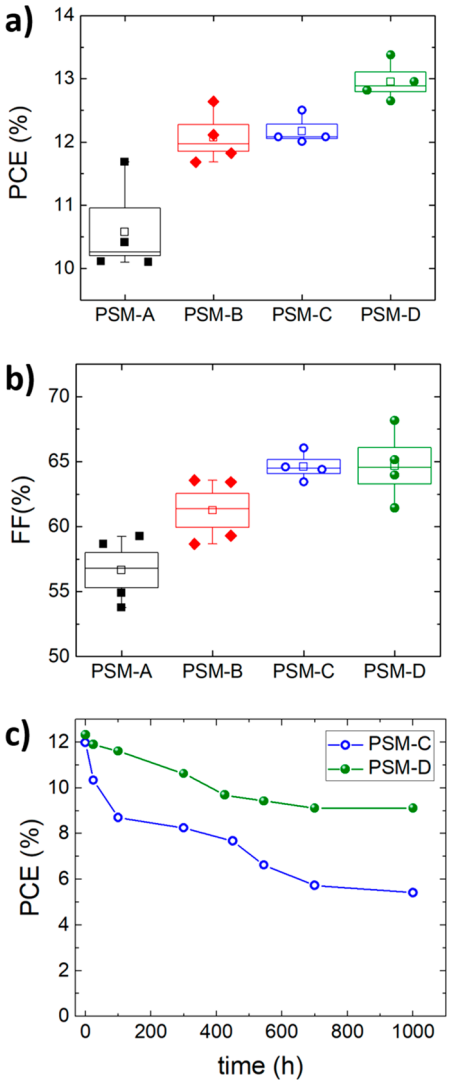

Figure 5. (a) PCE and (b) FF statistics for the various PSMs extracted by the corresponding $I-V$ characteristics under 1 sun illumination. (c) PCE trends vs time extracted by the $I-V$ characteristics under 1 sun illumination, periodically acquired during the prolonged thermal stress test at 65 °C (ISOS-D2) for PSM-C and PSM-D. The statistics were measured on four PSMs for each configuration.

Beyond chemically and electronically repairing the defective lattice of the MoS_2 flakes,[91] the MPA-based functionalization is effective to shift MoS_2 energy bands up (see characterization measurements in Figure S2). Actually, MPA has also been recently exploited to shift the energy bands of PbS quantum dots up,[93] offering a versatile tool to engineering the interfaces in optoelectronic devices.[83] In our case, as sketched in Figure 1b, the upshift of the MoS_2 energy bands has an immediate dual role: (1) to align the valence band edge of MoS_2 with the HOMO level of the perovskite, improving the hole extraction process,[93] and (2) to shift the conduction band edge of MoS_2 above the LUMO level of the perovskite, restricting undesired electron transfer (i.e., providing electron blocking properties).[30]

To assess the beneficial role of $fMoS_2$ as ABL, small-area devices (0.09 cm^2 active area) were fabricated using graphene-based ETLs without (reference sample) and with MoS_2 or $fMoS_2$ ABLs at the perovskite/HTM interface. Figure 2 reports the photovoltaic parameter statistics for the various PSCs extracted by the current−voltage ($I-V$) characteristics under 1 sun illumination.

Clearly, the insertion of the ABLs increases the PCE of the PSCs compared to the reference architectures. More in detail, the PCE increase is larger for cells with $fMoS_2$ (+11.6%) compared to that of MoS_2 cells (+3.7%). In fact, although the average J_{SC} increases for both ABL-based architectures (+4.8% and +7.2% for MoS_2 and $fMoS_2$, respectively) compared to reference devices, the FF and the V_{OC} relatively increase only for $fMoS_2$-based devices (+2% and +1%, respectively). Compared to both reference and MoS_2-based cells, in $fMoS_2$-based devices, the increase of FF is attributed to a well-balanced hole and electron extraction, while the correct energy alignment between the perovskite HOMO and the $fMoS_2$ valence band edge explains the increase of the average V_{OC}. Both these effects synergistically boost the PCE of the champion $fMoS_2$-based cell up to 19.2% (averaged PCE of 18.3%).

DOI: 10.1021/acsenergylett.9b01151
ACS Energy Lett. XXXX, XXX, XXX−XXX

The beneficial role of $fMoS_2$ into the device architecture was confirmed by both electrical and spectroscopic measurements. First, V_{OC} values were acquired by progressively increasing the incident power (P_{inc}) with a calibrated white LED, as shown in the V_{OC} vs $\log(P_{inc})$ plot (Figure 3a). In fact, the analysis of the latter allows the working mechanisms (i.e., charge generation/recombination/collection) of PSCs to be studied.[94] In particular, at low irradiance level (P_{inc} < 0.2 sun, region II) the slope of the V_{OC} vs $\log(P_{inc})$ plot is related to the electron *quasi*-Fermi level, which is determined by the charge accumulation and density of states in the ETL (i.e., $cTiO_2$ + $G/mTiO_2$ + G).[94] Consequently, the devices show almost the same V_{OC} slopes under such conditions. For larger P_{inc} (>0.2 sun, region III), the energy states of the ETL are fully filled, and the charge generation and recombination rates within the device determine the slope of the V_{OC} vs $\log(P_{inc})$ plot.[94] In particular, the slope increase (+7%) exhibited by the MoS_2-based device compared to the reference cell is attributed to an increase in the charge recombination rate at the perovskite/HTM interface. In fact, the presence of MoS_2 can activate additional recombination pathways compared to the bare spiro-OMeTAD,[89] causing a slight decrease (−0.3%) of the average V_{OC} (see Figure 2a). Interestingly, the devices using the $fMoS_2$ ABL show the lowest slope (98 mV dec^{-1}) of the V_{OC} vs $\log(P_{inc})$ plot in region III (Figure 3a). This indicates that the $fMoS_2$ ABL facilitates the hole transfer from the active layer to the HTM compared to both reference and MoS_2-based cells. Steady-state PL measurements were performed to further evaluate the capability of the $fMoS_2$ ABLs to extract the photogenerated holes from the perovskite. In fact, the hole-extraction process hinders the radiative charge recombination in the absorber material,[95,96] which then shows a PL quenching.[97] Figure 3b shows that the use of the $fMoS_2$ ABL reduces the PL emission of the perovskite. Quantitatively, the PL decreases by 9% in the presence of $fMoS_2$ ABL compared to the reference device. Thus, this result indicates that $fMoS_2$ ABLs effectively accelerate the hole-extraction dynamics at the photoelectrode. Transient photocurrent measurements can be additionally carried out to reveal information about the charge carrier transport within the PSCs.[98] Figure 3c reports the transient photocurrent profile recorded for both reference and $fMoS_2$-based devices. The data show fast rises of the photocurrent (in the order of μs), which are compatible with time scales associated with electron/hole transport.[99,100] Thus, the faster photocurrent rise in the case of the $fMoS_2$-based device compared to the reference indicates that the presence of the $fMoS_2$ ABL speeds up the hole charge collection toward the CE of the devices. This improves the charge collection efficiency, as also evidenced by incident-photon-to-current conversion efficiency (IPCE) spectroscopy measurements (Figure 3d). In particular, the integrated J_{SC} for $fMoS_2$-based cells increases by 4.8% compared to those of reference devices, in agreement with the J_{SC} values extrapolated by the $I-V$ characteristics under 1 sun illumination (Figure 2b). Overall, these data highlight the crucial role of the functionalization of MoS_2 for optimal engineering of the perovskite/ABL/HTM interface and increasing simultaneously the J_{SC} and the V_{OC} relative to those of reference devices.

Large-Area Modules. The upscaling of PSCs toward PSMs induces several performance losses, the most relevant ones related to the interfacial charge recombination and the interconnection of the multiple cells in a module.[101] In fact, on the one hand, it is critical to deposit the various PSM layers over a large area with the same quality reached as in small-area devices. Consequently, the interfacial charge recombination experimentally increases with the increase of the interfacial surface area. On the other hand, the typical PSM design consists of a monolithic series interconnection of rectangular subcells (with charge flowing across the smaller dimension),[102] since it effectively prevents an excessive increase of the series resistance of the FTO contact (whose sheet resistance is in the order of tens of Ω $\square^{-1}$).[102] However, the overall series resistance given by the other layers of the subcells still causes resistive losses, which decrease the FF and, thus, the power output of the PSMs.[103] In this context, the performance losses induced by the scaling-up process can be mitigated by the use of a 2D material engineered structure investigated for small-area devices, since it improves both the perovskite/CTL interface and the conductivity of the ETL. Following this rationale, the as-optimized mesoscopic PSCs were scaled up to large-area PSMs. The reference module architecture (i.e., without 2D materials) is hereafter named PSM-A. The structure based on the $cTiO_2/mTiO_2$+G layer and c-TiO_2+G/TiO_2+G are named PSM-B and PSM-C, respectively, while the fully optimized 2D material-engineered structure, including the $fMoS_2$ ABL, is named PSM-D. The detailed description of the PSM manufacturing is reported in the Supporting Information. Briefly, the module production requires several additional steps compared to that of small-area devices. These steps consist of patterning the module cells by four laser ablation processes.[83] In particular, a first laser ablation step (P1) selectively removes the FTO to isolate adjacent cells; a second laser ablation step (P2) removes the complete ETL/perovskite/(ABL)/spiro-OMeTAD stack to create the contact area between the cell vertical interconnection and the free FTO area. Lastly, a third ablation step (P3) isolates the adjacent cells by removing the Au CE. For P2, the power of a green laser (Nd:YVO_4, λ = 532 nm) was adjusted carefully by evaluating the perovskite absorbance and the eventual presence of 2D materials. First, PSM-C and PSM-D with an active area of 82 cm^2 were produced over a 12.5 × 12.5 cm^2 substrate. Such PSMs were obtained by 10 series-connected cells (single-cell active area of 8.2 cm^2). As shown in Figure S3 and Table S1, the as-produced $fMoS_2$-based module (PSM-D) shows a PCE of 15.27%, representing an improvement of 12.6% compared to the PCE of PSM-C (13.56%). In fact, the $fMoS_2$ ABL in PSM-D increases the module current (+3.9%) and FF (+8.3%) compared to PSM-C. To further scale-up the PSM active area from 82 to 108 cm^2, the PSM layout was optimized in terms of cell width and dead area between adjacent cells, leading to a final design consisting of 22 series-connected cells with a single-cell active area of 4.9 cm^2 and a final aperture ratio (defined as AR = AA/(AA + DA) in which AA is the active area and DA is the dead area) of 88%. More in detail, in such a PSM layout, the P1, P2, and P3 scribes are 40, 30, and 30 μm, respectively, while the safety area, i.e., the area between two adjacent laser scribes, is 135 μm. Figure 4a shows the photograph of an as-prepared large-area PSM. The $I-V$ characteristics of the champion devices for each PSM are reported in Figure 4b, evidencing the best photovoltaic performance for PSM-D, followed by PSM-C. The stabilized powers at maximum power point (P_{MPP}) for PSM-C and PSM-D are also reported in Figure 4c, indicating that the use of the $fMoS_2$-based ABL increases the P_{MPP} (+7.1%) compared to that of the PSM-C adopting the pristine MoS_2-based ABL.

DOI: 10.1021/acsenergylett.9b01151
ACS Energy Lett. XXXX, XXX, XXX−XXX

Figure 5a,b and Figure S4a,b report the photovoltaic parameter statistics for the various PSMs extracted by the $I-V$ characteristics under 1 sun illumination. The PCE progressively increases passing from PSM-A to PSM-D (Figure 5a), confirming the crucial role of 2D material-based interface engineering for boosting the photovoltaic performance. In particular, the FF of the module (Figure 5b) undergoes an improvement of 14% passing from an average value of 57% to 65% for PSM-A and PSM-D, respectively. This improvement can be attributed to the effect of 2D material-based interface engineering, since all the investigated modules were realized adopting the same optimized layout. Moreover, the V_{OC} and the J_{SC} improved passing from PSM-C to PSM-D (+3.64% and +3.9%, respectively; see Figure S4), thus confirming the trend observed on small-area PSCs (see Figure 2a,b).

Notably, the fully 2D-material engineered modules (i.e., PSM-D, comprising both graphene-based ETLs and $fMoS_2$-based ABLs) have shown an averaged PCE approaching 13%, with a record PCE of 13.4% and a record-high area-indexed aperture PCE (AIAPCE = AA × AR × PCE)[83] of 1266.5% cm^2.

Finally, stability tests were performed by applying to the PSMs prolonged thermal stress at 65 °C in an oven (ISOS-D2)[104] and recording the corresponding PCE as a function of the thermal stress time (Figure 5c). The $fMoS_2$-based module (PSM-D) exhibited a clear PCE stabilization, as evidenced by a remarkable improvement (+370 h) in the T_{80} lifetime (defined as the time span in which the device retains more than 80% of its initial efficiency) compared to the one of module PSM-C. Although a deeper investigation of the thermal-induced degradation mechanisms is still ongoing, we believe that the homogeneous $fMoS_2$ interlayer (as demonstrated in Figure S5) can be effective in (1) preventing the direct contact between the spiro-OMeTAD dopants and the perovskite surface, which promotes the interface degradation already experienced at 65 °C,[105] and (2) blocking atom migration from the Au electrode to the perovskite.[63]

In conclusion, we have demonstrated 2D-material-engineered PSMs with a PCE of 13.4% over an active area of 108 cm^2. This result, coupled with the superior thermal stability shown by 2D-based PSMs compared to reference devices, could pave the way for a feasible and reproducible scaling-up of perovskite-based photovoltaic technologies.

■ ASSOCIATED CONTENT

Supporting Information

The Supporting Information is available free of charge on the ACS Publications website at DOI: 10.1021/acsenergylett.9b01151.

Details on employed materials, cell and module fabrication, material characterizations, electro-optical measurement setup (IPCE, ARKEO, $I-V$ characteristics), and electrical characterization of the PSMs with both active areas of 82 cm^2 and 108 cm^2 (PDF)

■ AUTHOR INFORMATION

Corresponding Authors

*Aldo Di Carlo. E-mail: aldo.dicarlo@uniroma2.it.

*Francesco Bonaccorso. E-mail: francesco.bonaccorso@iit.it.

ORCID

Sara Pescetelli: 0000-0002-3336-2425

Alessandro Lorenzo Palma: 0000-0002-1682-7032

Mirko Prato: 0000-0002-2188-8059

Francesco Bonaccorso: 0000-0001-7238-9420

Aldo Di Carlo: 0000-0001-6828-2380

Author Contributions

¶(A.A. and S.P.) Both authors contributed equally to this work

Author Contributions

A.A., S.P., and A.D.C. conceived the work. A.A., S.P., A.L.P., and A.D.C. performed the experiments on small and large area devices, the electro-optical characterizations, and the stress test. S.P. created the ToC/abstract graphic. L.N., S.B., B.M.G., I.M., and F.B. produced and characterized the 2D materials. The manuscript was written through contributions of all authors. All authors have given approval to the final version of the manuscript.

Notes

The authors declare no competing financial interest.

■ ACKNOWLEDGMENTS

This Project has received funding from the European Union's Horizon 2020 research and innovation programme under Grant Agreement No. 696656 (GrapheneCore1), No. 785219 - GrapheneCore2, and Spearhead Project 3 "Graphene-perovskite solar farm" during the Core2 project. A.A. gratefully acknowledges the financial support from the Ministry of Education and Science of the Russian Federation in the framework of Increase Competitiveness Program of NUST ≪MISiS≫ (No. K3-2018-035), implemented by a governmental decree dated 16th of March 2013, N 211. The authors thank Michele Zarlenga (Officina meccanica, Dipartimento di Fisica Università di Roma "Tor Vergata") for technical support in the customization of the spin coater; A. E. del Rio Castillo and R. Oropesa-Nunez (Graphene Laboratories facility, Istituto Italiano di tecnologia, for useful discussion; the Materials Characterization facility, Istituto Italiano di Tecnologia, for support in AFM data acquisition; and Electron Microscopy facility, Istituto Italiano di Tecnologia, for support in TEM data acquisition.

■ REFERENCES

(1) Huang, F.; Li, M.; Siffalovic, P.; Cao, G.; Tian, J. From Scalable Solution Fabrication of Perovskite Films towards Commercialization of Solar Cells. *Energy Environ. Sci.* **2019**, *12* (2), 518−549.

(2) Green, M. A.; Ho-Baillie, A. Perovskite Solar Cells: The Birth of a New Era in Photovoltaics. *ACS Energy Lett.* **2017**, *2* (4), 822−830.

(3) https://www.nrel.gov/pv/assets/images/efficiency-chart.png (accessed on 27 May 2019).

(4) https://www.oxfordpv.com/news/oxford-pv-sets-world-record-perovskite-solar-cell (accessed on 27 May 2019).

(5) Raza, E.; Ahmad, Z.; Aziz, F. Stability of Organometal Halide Perovskite Solar Cells and Role of HTMs : Recent Developments And. *RSC Adv.* **2018**, *8*, 20952−20967.

(6) Yang, Z.; Zhang, S.; Li, L.; Chen, W. Research Progress on Large-Area Perovskite Thin Films and Solar Modules. *J. Mater.* **2017**, *3*, 231−244.

(7) Correa-Baena, J.-P.; Saliba, M.; Buonassisi, T.; Grätzel, M.; Abate, A.; Tress, W.; Hagfeldt, A. Promises and Challenges of Perovskite Solar Cells. *Science* **2017**, *358*, 739−744.

(8) Park, N. G.; Grätzel, M.; Miyasaka, T.; Zhu, K.; Emery, K. Towards Stable and Commercially Available Perovskite Solar Cells. *Nat. Energy* **2016**, *1* (11), 1−8.

(9) Wang, Q.; Chen, B.; Liu, Y.; Deng, Y.; Bai, Y.; Dong, Q.; Huang, J. Scaling Behavior of Moisture-Induced Grain Degradation in Polycrystalline Hybrid Perovskite Thin Films. *Energy Environ. Sci.* **2017**, *10* (2), 516−522.

DOI: 10.1021/acsenergylett.9b01151
ACS Energy Lett. XXXX, XXX, XXX−XXX

(10) Bryant, D.; Aristidou, N.; Pont, S.; Sanchez-Molina, I.; Chotchunangatchaval, T.; Wheeler, S.; Durrant, J. R.; Haque, S. A. Light and Oxygen Induced Degradation Limits the Operational Stability of Methylammonium Lead Triiodide Perovskite Solar Cells. *Energy Environ. Sci.* **2016**, *9*, 1655−1660.
(11) Aristidou, N.; Sanchez-Molina, I.; Chotchuangchutchaval, T.; Brown, M.; Martinez, L.; Rath, T.; Haque, S. A. The Role of Oxygen in the Degradation of Methylammonium Lead Trihalide Perovskite Photoactive Layers. *Angew. Chem., Int. Ed.* **2015**, *54* (28), 8208−8212.
(12) Nie, W.; Tsai, H.; Asadpour, R.; Blancon, J.-C.; Neukirch, A. J.; Gupta, G.; Crochet, J. J.; Chhowalla, M.; Tretiak, S.; Alam, M. A.; et al. Solar Cells. High-Efficiency Solution-Processed Perovskite Solar Cells with Millimeter-Scale Grains. *Science* **2015**, *347* (6221), 522−525.
(13) Conings, B.; Drijkoningen, J.; Gauquelin, N.; Babayigit, A.; D'Haen, J.; D'Olieslaeger, L.; Ethirajan, A.; Verbeeck, J.; Manca, J.; Mosconi, E.; et al. Intrinsic Thermal Instability of Methylammonium Lead Trihalide Perovskite. *Adv. Energy Mater.* **2015**, *5* (15), 1500477.
(14) Qiu, L.; Ono, L. K.; Qi, Y. Advances and Challenges to the Commercialization of Organic−inorganic Halide Perovskite Solar Cell Technology. *Mater. Today Energy* **2018**, *7*, 169−189.
(15) Juarez-Perez, E. J.; Hawash, Z.; Raga, S. R.; Ono, L. K.; Qi, Y. Thermal Degradation of $CH_3NH_3PbI_3$ Perovskite into NH_3 and CH_3I Gases Observed by Coupled Thermogravimetry-Mass Spectrometry Analysis. *Energy Environ. Sci.* **2016**, *9* (11), 3406−3410.
(16) Rong, Y.; Hu, Y.; Mei, A.; Tan, H.; Saidaminov, M. I.; Seok, S. Il; Mcgehee, M. D.; Sargent, E. H.; Han, H. Challenges for Commercializing Perovskite Solar Cells. *Science* **2018**, *361*, eaat8235.
(17) Li, Z.; Klein, T. R.; Kim, D. H.; Yang, M.; Berry, J. J.; Van Hest, M. F. A. M.; Zhu, K. Scalable Fabrication of Perovskite Solar Cells. *Nat. Rev. Mater.* **2018**, *3*, 1−20.
(18) Yang, M.; Li, Z.; Reese, M. O.; Reid, O. G.; Kim, D. H.; Siol, S.; Klein, T. R.; Yan, Y.; Berry, J. J.; Van Hest, M. F. A. M.; et al. Perovskite Ink with Wide Processing Window for Scalable High-Efficiency Solar Cells. *Nat. Energy* **2017**, *2* (5), 1−9.
(19) Jeon, N. J.; Noh, J. H.; Kim, Y. C.; Yang, W. S.; Ryu, S.; Seok, S. Solvent Engineering for High-Performance Inorganic-Organic Hybrid Perovskite Solar Cells. *Nat. Mater.* **2014**, *13* (July), 897.
(20) Xiao, M.; Huang, F.; Huang, W.; Dkhissi, Y.; Zhu, Y.; Etheridge, J.; Gray-Weale, A.; Bach, U.; Cheng, Y. B.; Spiccia, L. A Fast Deposition-Crystallization Procedure for Highly Efficient Lead Iodide Perovskite Thin-Film Solar Cells. *Angew. Chem., Int. Ed.* **2014**, *53* (37), 9898−9903.
(21) Deng, Y.; Zheng, X.; Bai, Y.; Wang, Q.; Zhao, J.; Huang, J. Surfactant-Controlled Ink Drying Enables High-Speed Deposition of Perovskite Films for Efficient Photovoltaic Modules. *Nat. Energy* **2018**, *3* (7), 560−566.
(22) Konstantakou, M.; Perganti, D.; Falaras, P.; Stergiopoulos, T. Anti-Solvent Crystallization Strategies for Highly Efficient Perovskite Solar Cells. *Crystals* **2017**, *7* (10), 291.
(23) Kim, J.; Yun, J. S.; Cho, Y.; Lee, D. S.; Wilkinson, B.; Soufiani, A. M.; Deng, X.; Zheng, J.; Shi, A.; Lim, S.; et al. Overcoming the Challenges of Large-Area High-Efficiency Perovskite Solar Cells. *ACS Energy Lett.* **2017**, *2* (9), 1978−1984.
(24) Razza, S.; Castro-Hermosa, S.; Di Carlo, A.; Brown, T. M. Research Update: Large-Area Deposition, Coating, Printing, and Processing Techniques for the Upscaling of Perovskite Solar Cell Technology. *APL Mater.* **2016**, *4* (9), 091508−091522.
(25) Li, J.; Munir, R.; Fan, Y.; Niu, T.; Liu, Y.; Zhong, Y.; Yang, Z.; Tian, Y.; Liu, B.; Sun, J.; et al. Phase Transition Control for High-Performance Blade-Coated Perovskite Solar Cells. *Joule* **2018**, *2* (7), 1313−1330.
(26) Kim, Y. Y.; Yang, T. Y.; Suhonen, R.; Välimäki, M.; Maaninen, T.; Kemppainen, A.; Jeon, N. J.; Seo, J. Gravure-Printed Flexible Perovskite Solar Cells: Toward Roll-to-Roll Manufacturing. *Adv. Sci.* **2019**, *6* (7), 1802094.
(27) Uličná, S.; Dou, B.; Kim, D. H.; Zhu, K.; Walls, J. M.; Bowers, J. W.; van Hest, M. F. A. M. Scalable Deposition of High-Efficiency Perovskite Solar Cells by Spray-Coating. *ACS Appl. Energy Mater.* **2018**, *1* (5), 1853−1857.
(28) Bishop, J. E.; Routledge, T. J.; Lidzey, D. G. Advances in Spray-Cast Perovskite Solar Cells. *J. Phys. Chem. Lett.* **2018**, *9* (8), 1977−1984.
(29) Park, M.; Cho, W.; Lee, G.; Hong, S. C.; Kim, M.-c.; Yoon, J.; Ahn, N.; Choi, M. Highly Reproducible Large-Area Perovskite Solar Cell Fabrication via Continuous Megasonic Spray Coating of $CH_3NH_3PbI_3$. *Small* **2019**, *15* (1), 1804005.
(30) Najafi, L.; Taheri, B.; Martín-García, B.; Bellani, S.; Di Girolamo, D.; Agresti, A.; Oropesa-Nuñez, R.; Pescetelli, S.; Vesce, L.; Calabrò, E.; et al. MoS_2 Quantum Dot/Graphene Hybrids for Advanced Interface Engineering of a $CHNH_3PbI_3$ Perovskite Solar Cell with an Efficiency of over 20%. *ACS Nano* **2018**, *12* (11), 10736−10754.
(31) Yang, G.; Wang, C.; Lei, H.; Zheng, X.; Qin, P.; Xiong, L.; Zhao, X.; Yan, Y.; Fang, G. Interface Engineering in Planar Perovskite Solar Cells: Energy Level Alignment, Perovskite Morphology Control and High Performance Achievement. *J. Mater. Chem. A* **2017**, *5* (4), 1658−1666.
(32) Bai, Y.; Meng, X.; Yang, S. Interface Engineering for Highly Efficient and Stable Planar P-i-n Perovskite Solar Cells. *Adv. Energy Mater.* **2018**, *8* (5), 1701883.
(33) Grancini, G.; Roldàn-Carmona, C.; Zimmermann, I.; Mosconi, E.; Lee, X.; Martineau, D.; Narbey, S.; Oswald, F.; De Angelis, F.; Graetzel, M.; Nazeeruddin, M. K. One-Year stable perovskite solar cells by 2D/3D Interface Engineering. *Nat. Commun.* **2017**, *8*, 15684.
(34) Zhao, L.; Kerner, R. A.; Xiao, Z.; Lin, Y. L.; Lee, K. M.; Schwartz, J.; Rand, B. P. Redox Chemistry Dominates the Degradation and Decomposition of Metal Halide Perovskite Optoelectronic Devices. *ACS Energy Lett.* **2016**, *1* (3), 595−602.
(35) Zhou, H.; Chen, Q.; Li, G.; Luo, S.; Song, T.; Duan, H.-S.; Hong, Z.; You, J.; Liu, Y.; Yang, Y. Interface Engineering of Highly Efficient Perovskite Solar Cells. *Science* **2014**, *345* (6196), 542−546.
(36) Seo, Y.; Kim, E.; Cho, S.; Kim, S.; Na, S. High-Performance Planar Perovskite Solar Cells : Influence of Solvent upon Performance. *Appl. Mater. Today* **2017**, *9*, 598−604.
(37) Jung, E. H.; Jeon, N. J.; Park, E. Y.; Moon, C. S.; Shin, T. J.; Yang, T. Y.; Noh, J. H.; Seo, J. Efficient, Stable and Scalable Perovskite Solar Cells Using Poly(3-Hexylthiophene). *Nature* **2019**, *567* (7749), 511−515.
(38) Chen, W.; Yin, X.; Que, M.; Xie, H.; Liu, J.; Yang, C.; Guo, Y.; Wu, Y.; Que, W. A Comparative Study of Planar and Mesoporous Perovskite Solar Cells with Printable Carbon Electrodes. *J. Power Sources* **2019**, *412*, 118−124.
(39) Dagar, J.; Castro-Hermosa, S.; Gasbarri, M.; Palma, A. L.; Cina, L.; Matteocci, F.; Calabrò, E.; Di Carlo, A.; Brown, T. M. Efficient Fully Laser-Patterned Flexible Perovskite Modules and Solar Cells Based on Low-Temperature Transport Layers. *Nano Res.* **2018**, *11*, 2669−2681.
(40) Bu, T.; Li, J.; Zheng, F.; Chen, W.; Wen, X.; Ku, Z.; Peng, Y.; Zhong, J.; Cheng, Y. B.; Huang, F. Universal Passivation Strategy to Slot-Die Printed SnO_2 for Hysteresis-Free Efficient Flexible Perovskite Solar Module. *Nat. Commun.* **2018**, *9* (1), 1−10.
(41) Calabrò, E.; Matteocci, F.; Palma, A. L.; Vesce, L.; Taheri, B.; Carlini, L.; Pis, I.; Nappini, S.; Dagar, J.; Battocchio, C.; et al. Solar Energy Materials and Solar Cells Low Temperature, Solution-Processed Perovskite Solar Cells and Modules with an Aperture Area Efficiency of 11%. *Sol. Energy Mater. Sol. Cells* **2018**, *185*, 136−144.
(42) Christians, J. A.; Schulz, P.; Tinkham, J. S.; Schloemer, T. H.; Harvey, S. P.; Tremolet De Villers, B. J.; Sellinger, A.; Berry, J. J.; Luther, J. M. Tailored Interfaces of Unencapsulated Perovskite Solar Cells for > 1,000 h Operational Stability. *Nat. Energy* **2018**, *3* (1), 68−74.
(43) Christians, J. A.; Zhang, F.; Bramante, R. C.; Reese, M. O.; Schloemer, T. H.; Sellinger, A.; Van Hest, M. F. A. M.; Zhu, K.; Berry, J. J.; Luther, J. M. Stability at Scale: Challenges of Module

DOI: 10.1021/acsenergylett.9b01151
ACS Energy Lett. XXXX, XXX, XXX−XXX

Interconnects for Perovskite Photovoltaics. *ACS Energy Lett.* **2018**, *3* (10), 2502−2503.
(44) Yang, M.; Kim, D. H.; Klein, T. R.; Li, Z.; Reese, M. O.; Tremolet de Villers, B. J.; Berry, J. J.; van Hest, M. F. A. M.; Zhu, K. Highly Efficient Perovskite Solar Modules by Scalable Fabrication and Interconnection Optimization. *ACS Energy Lett.* **2018**, *3*, 322−328.
(45) Di Giacomo, F.; Shanmugam, S.; Fledderus, H.; Bruijnaers, B. J.; Verhees, W. J. H.; Dorenkamper, M. S.; Veenstra, S. C.; Qiu, W.; Gehlhaar, R.; Merckx, T.; et al. Up-Scalable Sheet-to-Sheet Production of High Efficiency Perovskite Module and Solar Cells on 6-in. Substrate Using Slot Die Coating. *Sol. Energy Mater. Sol. Cells* **2018**, *181*, 53−59.
(46) Hong, S.; Lee, J.; Kang, H.; Kim, G.; Kee, S.; Lee, J.; Jung, S.; Park, B.; Kim, S.; Back, H.; et al. High-Efficiency Large-Area Perovskite Photovoltaic Modules Achieved via Electrochemically Assembled Metal-Filamentary Nanoelectrodes. *Sci. Adv.* **2018**, *4*, eaat3604.
(47) Hu, Y.; Si, S.; Mei, A.; Rong, Y.; Liu, H.; Li, X.; Han, H. Stable Large-Area (10×10 Cm ^{2}) Printable Mesoscopic Perovskite Module Exceeding 10% Efficiency. *Sol. RRL* **2017**, *1* (2), 1600019.
(48) Duan, M.; Hu, Y.; Mei, A.; Rong, Y.; Han, H. Printable Carbon-Based Hole-Conductor-Free Mesoscopic Perovskite Solar Cells: From Lab to Market. *Mater. Today Energy* **2018**, *7*, 221−231.
(49) Chen, H.; Yang, S. Carbon-Based Perovskite Solar Cells without Hole Transport Materials: The Front Runner to the Market? *Adv. Mater.* **2017**, *29* (24), 1603994−1604010.
(50) De Rossi, F.; Baker, J. A.; Beynon, D.; Hooper, K. E. A.; Meroni, S. M. P.; Williams, D.; Wei, Z.; Yasin, A.; Charbonneau, C.; Jewell, E. H.; et al. All Printable Perovskite Solar Modules with 198 Cm 2 Active Area and Over 6% Efficiency. *Adv. Mater. Technol.* **2018**, *3*, 1800156.
(51) Balis, N.; Stratakis, E.; Kymakis, E. Graphene and Transition Metal Dichalcogenide Nanosheets as Charge Transport Layers for Solution Processed Solar Cells. *Mater. Today* **2016**, *19* (10), 580−594.
(52) Kakavelakis, G.; Kymakis, E.; Petridis, K. 2D Materials Beyond Graphene for Metal Halide Perovskite Solar Cells. *Adv. Mater. Interfaces* **2018**, *5*, 1800339.
(53) Agresti, A.; Pescetelli, S.; Palma, A. L.; Del Rio Castillo, A. E.; Konios, D.; Kakavelakis, G.; Razza, S.; Cina, L.; Kymakis, E.; et al. Graphene Interface Engineering for Perovskite Solar Modules: 12.6% Power Conversion Efficiency over 50 Cm^2 Active Area. *ACS Energy Lett.* **2017**, *2* (1), 279−287.
(54) Agresti, A.; Pescetelli, S.; Taheri, B.; Del Rio Castillo, A. E.; Cinà, L.; Bonaccorso, F.; Di Carlo, A. Graphene-Perovskite Solar Cells Exceed 18% Efficiency: A Stability Study. *ChemSusChem* **2016**, *9* (18), 2609−2619.
(55) Biccari, F.; Gabelloni, F.; Burzi, E.; Gurioli, M.; Pescetelli, S.; Agresti, A.; Del Rio Castillo, A. E.; Ansaldo, A.; Kymakis, E.; Bonaccorso, F.; et al. Graphene-Based Electron Transport Layers in Perovskite Solar Cells: A Step-Up for an Efficient Carrier Collection. *Adv. Energy Mater.* **2017**, *7*, 1701349.
(56) Palma, A. L.; Cinà, L.; Pescetelli, S.; Agresti, A.; Raggio, M.; Paolesse, R.; Bonaccorso, F.; Di Carlo, A. Reduced Graphene Oxide as Efficient and Stable Hole Transporting Material in Mesoscopic Perovskite Solar Cells. *Nano Energy* **2016**, *22*, 349−360.
(57) Agresti, A.; Pescetelli, S.; Cinà, L.; Konios, D.; Kakavelakis, G.; Kymakis, E.; Carlo, A. Di. Efficiency and Stability Enhancement in Perovskite Solar Cells by Inserting Lithium-Neutralized Graphene Oxide as Electron Transporting Layer. *Adv. Funct. Mater.* **2016**, *26*, 2686−2694.
(58) Busby, Y.; Agresti, A.; Pescetelli, S.; Di Carlo, A.; Noel, C.; Pireaux, J.; Houssiau, L. Aging Effects in Interface-Engineered Perovskite Solar Cells with 2D Nanomaterials : A Depth pro Fi Le Analysis. *Mater. Today Energy* **2018**, *9*, 1−10.
(59) Ahn, N.; Kwak, K.; Jang, M. S.; Yoon, H.; Lee, B. Y.; Lee, J.; Pikhitsa, P. V.; Byun, J.; Choi, M. Trapped Charge-Driven Degradation of Perovskite Solar Cells. *Nat. Commun.* **2016**, *7*, 13422.
(60) Asghar, M. I.; Zhang, J.; Wang, H.; Lund, P. D. Device Stability of Perovskite Solar Cells − A Review. *Renew. Sustain. Energy Rev.* **2017**, *77*, 131−146.
(61) Arora, N.; Dar, M. I.; Hinderhofer, A.; Pellet, N.; Schreiber, F.; Zakeeruddin, S. M.; Grätzel, M. Perovskite Solar Cells with CuSCN Hole Extraction Layers Yield Stabilized Efficiencies Greater than 20%. *Science* **2017**, *358*, 768−771.
(62) Brunetti, B.; Cavallo, C.; Ciccioli, A.; Gigli, G.; Latini, A. On the Thermal and Thermodynamic (In) Stability of Methylammonium Lead Halide Perovskites. *Sci. Rep.* **2016**, *6*, 1−12.
(63) Domanski, K.; Mine, N.; Nazeeruddin, M. K.; Abate, A.; Saliba, M.; Tress, W.; Hagfeldt, A.; Grätzel, M.; Correa-Baena, J.-P. Not All That Glitters Is Gold : Metal Migration- Induced Degradation in Perovskite Solar Cells. *ACSNano* **2016**, *10* (6), 6306−6314.
(64) Walsh, A.; Stranks, S. D. Taking Control of Ion Transport in Halide Perovskite Solar Cells. *ACS Energy Lett.* **2018**, *3* (8), 1983−1990.
(65) Li, C.; Guerrero, A.; Huettner, S.; Bisquert, J. Unravelling the Role of Vacancies in Lead Halide Perovskite through Electrical Switching of Photoluminescence. *Nat. Commun.* **2018**, *9* (1), 1−8.
(66) Kim, N.; Min, Y. H.; Noh, S.; Cho, E.; Jeong, G.; Ahn, S.; Lee, J. S.; Kim, S.; Ihm, K.; Ahn, H.; et al. Investigation of Thermally Induced Degradation in $CH_3NH_3PbI_3$ Perovskite Solar Cells Using In-Situ Synchrotron Radiation Analysis. *Sci. Rep.* **2017**, *7* (March), 1−9.
(67) Saliba, M.; Matsui, T.; Seo, J.-Y.; Domanski, K.; Correa-Baena, J.-P.; Nazeeruddin, M. K.; Zakeeruddin, S. M.; Tress, W.; Abate, A.; Hagfeldt, A.; et al. Cesium-Containing Triple Cation Perovskite Solar Cells: Improved Stability, Reproducibility and High Efficiency. *Energy Environ. Sci* **2016**, *9*, 1989−1997.
(68) Jung, M.; Kim, C.; Jeon, J.; Yang, S.; Seo, J.; Noh, J. H.; Il Seok, S. Thermal Stability of CuSCN Hole Conductor-Based Perovskite Solar Cells. *ChemSusChem* **2016**, *9*, 2592−2596.
(69) Rolston, N.; Watson, B. L.; Bailie, C. D.; Mcgehee, M. D.; Bastos, J. P.; Gehlhaar, R.; Kim, J.; Vak, D.; Mallajosyula, A. T.; Gupta, G.; et al. Mechanical Integrity of Solution-Processed Perovskite Solar Cells. *Extrem. Mech. Lett.* **2016**, *9*, 353−358.
(70) Hawash, Z.; Ono, L. K.; Qi, Y. Recent Advances in Spiro-MeOTAD Hole Transport Material and Its Applications in Organic − Inorganic Halide Perovskite Solar Cells. *Adv. Mater.* **2018**, *5*, 1700623.
(71) Wang, S.; Sina, M.; Parikh, P.; Uekert, T.; Shahbazian, B.; Devaraj, A.; Meng, Y. S. Role of 4- *Tert* -Butylpyridine as a Hole Transport Layer Morphological Controller in Perovskite Solar Cells. *Nano Lett.* **2016**, *16* (9), 5594−5600.
(72) Snaith, H. J.; Grätzel, M. Enhanced Charge Mobility in a Molecular Hole Transporter via Addition of Redox Inactive Ionic Dopant: Implication to Dye-Sensitized Solar Cells. *Appl. Phys. Lett.* **2006**, *89* (26), 262114−262117.
(73) Nguyen, W. H.; Bailie, C. D.; Unger, E. L.; Mcgehee, M. D. Enhancing the Hole-Conductivity of Spiro-OMeTAD without Oxygen or Lithium Salts by Using Spiro(TFSI)$_2$ in Perovskite and Dye- Sensitized Solar Cells. *J. Am. Chem. Soc.* **2014**, *136*, 10996−11001.
(74) Liu, J.; Wu, Y.; Qin, C.; Yang, X.; Yasuda, T.; Islam, A.; Zhang, K.; Peng, W.; Chen, W.; Han, L. A Dopant-Free Hole-Transporting Material for Efficient and Stable Perovskite Solar Cells. *Energy Environ. Sci.* **2014**, *7* (9), 2963−2967.
(75) Sanchez, R. S.; Mas-Marza, E. Light-Induced Effects on Spiro-OMeTAD Films and Hybrid Lead Halide Perovskite Solar Cells. *Sol. Energy Mater. Sol. Cells* **2016**, *158*, 189−194.
(76) Jena, A. K.; Ikegami, M.; Miyasaka, T. Severe Morphological Deformation of Spiro-OMeTAD in $(CH_3NH_3)PbI_3$ Solar Cells at High Temperature. *ACS Energy Lett.* **2017**, *2* (8), 1760−1761.
(77) Graetzel, M. Photoelectrochemical Cells. *Nature* **2001**, *414*, 338−344.
(78) Chung, I.; Lee, B.; He, J.; Chang, R. P. H.; Kanatzidis, M. G. All-Solid-State Dye-Sensitized Solar Cells with High Efficiency. *Nature* **2012**, *485*, 486−490.

DOI: 10.1021/acsenergylett.9b01151
ACS Energy Lett. XXXX, XXX, XXX−XXX

(79) Kwon, K. C.; Choi, K. S.; Kim, S. Y. Increased Work Function in Few-Layer Graphene Sheets via Metal Chloride Doping. *Adv. Funct. Mater.* **2012**, *22* (22), 4724−4731.
(80) Hu, C.; Bai, Y.; Xiao, S.; Zhang, T.; Meng, X.; Ng, W. K.; Yang, Y.; Wong, K. S.; Chen, H.; Yang, S. Tuning A-Site Cation Composition of FA Perovskite for Efficient And. *J. Mater. Chem. A* **2017**, *5*, 21858−21865.
(81) Jiang, Y.; Leyden, M. R.; Qiu, L.; Wang, S.; Ono, L. K.; Wu, Z.; Juarez-perez, E. J.; Qi, Y. Combination of Hybrid CVD and Cation Exchange for Upscaling Cs-Substituted Mixed Cation Perovskite Solar Cells with High Efficiency and Stability. *Adv. Funct. Mater.* **2018**, *28*, 1703835.
(82) Schulz, P.; Edri, E.; Kirmayer, S.; Hodes, G.; Cahen, D.; Kahn, A. Interface Energetics in Organo-Metal Halide Perovskite-Based Photovoltaic Cells. *Energy Environ. Sci.* **2014**, *7* (4), 1377−1381.
(83) Palma, A. L.; Matteocci, F.; Agresti, A.; Pescetelli, S.; Calabro, E.; Vesce, L.; Christiansen, S.; Schmidt, M.; Di Carlo, A. Laser-Patterning Engineering for Perovskite Solar Modules With 95% Aperture Ratio. *IEEE J. Photovoltaics* **2017**, *7*, 1674−1680.
(84) Agresti, A.; Pescetelli, S.; Najafi, L.; Castillo, A. E. D. R.; Busby, Y.; Di Carlo, A. Graphene and Related 2D Materials for High Efficient and Stable Perovskite Solar Cells. In *Proceedings of the 17th IEEE International Conference on Nanotechnology Pittsburgh*; 2017; pp 145−150.
(85) Volonakis, G.; Giustino, F. Ferroelectric Graphene-Perovskite Interfaces. *J. Phys. Chem. Lett.* **2015**, *6* (13), 2496−2502.
(86) Huang, P.; Wang, Z.; Liu, Y.; Zhang, K.; Yuan, L.; Zhou, Y.; Song, B.; Li, Y. Water-Soluble 2D Transition Metal Dichalcogenides as Hole Transport Layer for High Efficient and Stable p-i-n Perovskite Solar Cells. *ACS Appl. Mater. Interfaces* **2017**, *9* (30), 25323−25331.
(87) Kim, Y. G.; Kwon, K. C.; Le, Q. V.; Hong, K.; Jang, H. W.; Kim, S. Y. Atomically Thin Two-Dimensional Materials as Hole Extraction Layers in Organolead Halide Perovskite Photovoltaic Cells. *J. Power Sources* **2016**, *319*, 1−8.
(88) Dasgupta, U.; Chatterjee, S.; Pal, A. J. Thin- Film Formation of 2D MoS_2 and Its Application as a Hole-Transport Layer in Planar Perovskite Solar Cells. *Sol. Energy Mater. Sol. Cells* **2017**, *172* (April), 353−360.
(89) Capasso, A.; Matteocci, F.; Najafi, L.; Prato, M.; Buha, J.; Cinà, L.; Pellegrini, V.; Di Carlo, A.; Bonaccorso, F. Few-Layer MoS_2 Flakes as Active Buffer Layer for Stable Perovskite Solar Cells. *Adv. Energy Mater.* **2016**, *6* (16), 1600920.
(90) Chen, X.; Berner, N. C.; Backes, C.; Duesberg, G. S.; McDonald, A. R. Functionalization of Two-Dimensional MoS_2: On the Reaction between MoS_2 and Organic Thiols. *Angew. Chem., Int. Ed.* **2016**, *55* (19), 5803−5808.
(91) Förster, A.; Gemming, S.; Seifert, G.; Tománek, D. Chemical and Electronic Repair Mechanism of Defects in MoS_2 Monolayers. *ACS Nano* **2017**, *11* (10), 9989−9996.
(92) Ding, Q.; Czech, K. J.; Zhao, Y.; Zhai, J.; Hamers, R. J.; Wright, J. C.; Jin, S. Basal-Plane Ligand Functionalization on Semiconducting 2H-MoS_2 Monolayers. *ACS Appl. Mater. Interfaces* **2017**, *9* (14), 12734−12742.
(93) Brown, P. R.; Kim, D.; Lunt, R. R.; Zhao, N.; Bawendi, M. G.; Grossman, J. C.; Bulović, V. Energy Level Modification in Lead Sulfide Quantum Dot Thin Films through Ligand Exchange. *ACS Nano* **2014**, *8* (6), 5863−5872.
(94) Gouda, L.; Gottesman, R.; Ginsburg, A.; Keller, D. A.; Haltzi, E.; Hu, J.; Tirosh, S.; Anderson, A. Y.; Zaban, A.; Boix, P. P. Open Circuit Potential Build-Up in Perovskite Solar Cells from Dark Conditions to 1 Sun. *J. Phys. Chem. Lett.* **2015**, *6*, 4640−4645.
(95) Bhosale, J. S.; Moore, J. E.; Wang, X.; Bermel, P.; Lundstrom, M. S. Steady-State Photoluminescent Excitation Characterization of Semiconductor Carrier Recombination. *Rev. Sci. Instrum.* **2016**, *87* (1), 013104−013111.
(96) Jiménez-López, J.; Cambarau, W.; Cabau, L.; Palomares, E. Charge Injection, Carriers Recombination and HOMO Energy Level Relationship in Perovskite Solar Cells. *Sci. Rep.* **2017**, *7* (1), 1−10.
(97) Wang, X.; Bhosale, J.; Moore, J.; Kapadia, R.; Bermel, P.; Javey, A.; Lundstrom, M. Photovoltaic Material Characterization with Steady State and Transient Photoluminescence. *IEEE J. Photovoltaics* **2015**, *5* (1), 282−287.
(98) Alsari, M.; Pearson, A. J.; Wang, J. T.; Wang, Z.; Greenham, N. C.; Snaith, H. J.; Lilliu, S.; Friend, R. H.; Montisci, A. Degradation Kinetics of Inverted Perovskite Solar Cells. *Sci. Rep.* **2018**, *8*, 5977.
(99) Pearson, A. J.; Hopkinson, P. E.; Couderc, E.; Domanski, K.; Abdi-jalebi, M.; Greenham, N. C. Critical Light Instability in CB/DIO Processed PBDTTT-EFT:$PC_{71}BM$ Organic Photovoltaic Devices. *Org. Electron.* **2016**, *30*, 225−236.
(100) Li, Z.; Gao, F.; Greenham, N. C.; Mcneill, C. R. Comparison of the Operation of Polymer/Fullerene, Polymer/Polymer, and Polymer/Nanocrystal Solar Cells : A Transient Photocurrent and Photovoltage Study. *Adv. Funct. Mater.* **2011**, *21* (8), 1419−1431.
(101) Razza, S.; Di Giacomo, F.; Matteocci, F.; Cinà, L.; Palma, A. L.; Casaluci, S.; Cameron, P.; D'Epifanio, A.; Licoccia, S.; Reale, A.; et al. Perovskite Solar Cells and Large Area Modules (100 Cm 2) Based on an Air Flow-Assisted PbI 2 Blade Coating Deposition Process. *J. Power Sources* **2015**, *277* (2015), 286−291.
(102) Bartlome, R.; Strahm, B.; Sinquin, Y.; Feltrin, A.; Ballif, C. Laser Applications in Thin-Film Photovoltaics. *Appl. Phys. B: Lasers Opt.* **2010**, *100* (2), 427−436.
(103) Rakocevic, L.; Gehlhaar, R.; Merckx, T.; Qiu, W.; Paetzold, U. W.; Fledderus, H.; Poortmans, J. Interconnection Optimization for Highly Efficient Perovskite Modules. *IEEE J. Photovoltaics* **2017**, *7* (1), 404−408.
(104) Reese, M. O.; Gevorgyan, S. A.; Jørgensen, M.; Bundgaard, E.; Kurtz, S. R.; Ginley, D. S.; Olson, D. C.; Lloyd, M. T.; Morvillo, P.; Katz, E. A.; et al. Consensus Stability Testing Protocols for Organic Photovoltaic Materials and Devices. *Sol. Energy Mater. Sol. Cells* **2011**, *95* (5), 1253−1267.
(105) Divitini, G.; Cacovich, S.; Matteocci, F.; Di Carlo, A.; Ducati, C.; Cinà, L. In Situ Observation of Heat-Induced Degradation of Perovskite Solar Cells. *Nat. Energy* **2016**, *1*, 15012.

DOI: 10.1021/acsenergylett.9b01151
ACS Energy Lett. XXXX, XXX, XXX−XXX